

# Towards Improving the Type IV Cracking Resistance in Cr-Mo Steel Weld Through Thermo-Mechanical Processing

\* Benjamin Shassere<sup>1</sup>, Yukinori Yamamoto<sup>2</sup>, Sudarsanam Suresh Babu<sup>1</sup>

<sup>1</sup>Department of Mechanical, Aerospace, and Biomedical Engineering, the University of Tennessee, Knoxville, TN 37996, USA

<sup>2</sup>Materials Science and Technology Division, Oak Ridge National Laboratory, Oak Ridge, TN 37831, USA

\*Corresponding author: bashassere21@gmail.com

## Abstract

Detailed microstructure characterization of Grade 91 (Modified 9Cr-1Mo, ASTM A387) steel subjected to a thermo-mechanical treatment (TMT) process was performed to rationalize the cross-weld creep properties. A series of thermo-mechanical processing in the austenite phase region, followed by isothermal aging at temperatures at 973 to 1173 K (700 to 900°C) was applied to the Grade 91 steel to promote precipitation kinetics of MX (M: Nb and V, X: C and N) in the austenite matrix. **Detailed characterization of the base metals after standard tempering confirmed the presence of fine MX dispersion within the tempered martensitic microstructure in steels processed at/and above 1073 K (800 °C).** Relatively low volume fraction of  $M_{23}C_6$  precipitates was observed after processing at 1073 K (800 °C). The cross-weld creep strength after processing was increased with respect to the increase of MX dispersion, **indicating that these MX precipitates maintained during weld thermal cycles in the fine grained heat affected zone (FGHAZ) region and thereby contribute to improved creep resistant of welds in comparison to the welds made with the standard “normalization and tempering” processes.** The steels processed in this specific processing condition showed improved cross-weld creep resistance and sufficient room-temperature toughness. The above data is also analysed based on existing theories of creep deformation based on dislocation climb mechanism.

*This manuscript has been authored by UT-Battelle, LLC under Contract No. DE-AC05-00OR22725 with the U.S. Department of Energy. The United States Government retains and the publisher, by accepting the article for publication, acknowledges that the United States Government retains a non-exclusive, paid-up, irrevocable, world-wide license to publish or reproduce the published form of this manuscript, or allow others to do so, for United States Government purposes. The Department of Energy will provide public access to these results of federally sponsored research in accordance with the DOE Public Access Plan (<http://energy.gov/downloads/doe-public-access-plan>).*

## ***1. Introduction***

With environmental concerns on the forefront of policymaking, it is important to implement any positive advance in emissions savings. In today's modern fossil fuel power plants, CO<sub>2</sub> emissions have the possibility for immediate reductions. Creep strength-enhanced ferritic (CSEF) steels containing 9-12Cr have been used in coal-fired boilers, heat-recovery steam generators because of their enhanced creep properties at high temperatures [1, 2]. The 9-12Cr steels, with enhanced creep properties allows for steam temperature and pressure to 923 K (650 °C) and 34.3 MPa [3]. However, the creep resistances of the grade 91 steel welds are inferior when compared to the base metal. There are reports of failures of these steel weldments after only a few years in service [4-9]. These failures have been credited to the non-equilibrium microstructures in FGHAZ regions, described elsewhere [7-9]. The premature failures at the FGHAZ are called "Type-IV cracking" [9-11]. The authors have briefly shown elsewhere that strengthening of the FGHAZ is key to improve the performance of CSEF steels.[12]

Yu et al. recently reported that applying a relatively lower pre-weld tempering temperature (e.g. 890-923 K (617-650 °C)) improved cross-weld creep properties of Grade 91 (Modified 9Cr-1Mo, ASTM A387) steel after a standard (e.g. 1033 K (760 °C)) post-weld heat treatment (PWHT) compared to that of materials that applied a standard pre-weld tempering (e.g. 1033 K (760 °C)) [13, 14]. Based on these findings, it was concluded that ensuing fine size distribution of M<sub>23</sub>C<sub>6</sub> in the FGHAZ after PWHT is the key to improve the cross-weld creep properties of the CSEF steels [6, 14]. Interestingly, the authors reported that the base metal subjected to a lower pre-weld tempering temperature, exhibited poor room temperature toughness, as well as, higher ductile to brittle transition temperature (353 K (80 °C)) compared to that of standard tempering samples (233 K(-40 °C)). Since ASTM standards calls for a minimum toughness level at room temperature, the "half-tempered" condition of the lower pre-weld tempering temperature, makes it nonviable for industrial adoption [11]. The objectives of the current research are to develop a thermo-mechanical (TMT) route that can induce fine distribution of precipitate, as well as, yield acceptable room temperature toughness for industrial acceptance.

Klueh et al. have reported a breakthrough concept for improving the creep properties of 9-12Cr CSEF steels through a thermo-mechanical treatment (TMT), which combines an hot-deformation in a temperature range where austenite is stable (aus-forming) and applying

subsequent isothermal annealing in the same temperature range (aus-aging) [15, 16]. By applying the TMT, the density of dislocations in the austenite matrix is increased which could act as nucleation sites for MX (M: mainly Nb and V, X: C, N). Subsequent aus-aging results in dense MX precipitation in the austenite before the matrix transforms to ferrite at high temperature or martensite on cooling to room temperature. The authors reported the material exhibiting almost two to three orders of magnitude longer creep life at 923 K (650 °C) and 138 MPa after deformations of 20-60% [15, 16]. Although the study focused only on the base metal properties, suitability of this route to improve creep properties of cross-weld samples have never been attempted. Our hypothesis is that such pre-existing MX precipitates will also be stable during welding process at the FGHAZ and thereby improve the creep resistance of the FGHAZ region [17, 18]. It should also be emphasized that the TMT process has the added benefit of the improved high-temperature strength, even after applying a standard tempering. Furthermore, the standard tempering may also lead to good room temperature ductility, as well. The innovative TMT concept could be a worthwhile route for a potential improvement of high temperature creep properties of Grade 91 welds, and forms the underlying motivation for the current research paper. In order to optimize the TMT process, the mechanisms of improved creep enhancements in welded materials need to be correlated to underlying microstructure and creep mechanisms and correlate the same to creep mechanisms.

## ***2. Experimental Procedures***

The composition of the Grade 91 steel used in the present study is shown in Table 1. Several small pieces (50-100 mm x 150-250mm x 25mm) were sectioned from a 25mm-thickness hot-rolled plate prepared in a previous study [9]. Aus-forging and subsequent aus-aging were applied to the Grade 91 steel plates in various conditions. The samples were heated to 1323 K (1050 °C) and held for 1h in Ar gas atmosphere, followed by air-cooling to an intermediate temperature in the range between 973 and 1173 K (700 and 900 °C) [below  $A_1$  (1093 K (820 °C)) or above the  $A_3$  (1133 K (860 °C)), respectively, and significantly higher than the  $M_s$  at 673 K (400°C)] [9]. On cooling to an intermediate temperature, a 7% thickness reduction was achieved by forging with only one press-stroke action. The aim of this low straining (7%), in contrast to higher than 20% used by Klueh et al. is to maintain parameters which more closely aligns in traditional manufacturing [15, 16]. After the thickness reduction, the plates were subsequently placed in a furnace for 1 h at the same temperature of the hot-working, and then air-cooled to RT. A second set of samples were then tempered at 1033 K ((760 °C))

for 2h. Figure 1 shows the temperature profiles of the Grade 91 samples during the TMT at 973, 1073, and 1173 K (700, 800, and 900 °C).

Manual gas tungsten arc weld (GTAW) was used to make cross weld samples from these plates with or without the filler metal. These welds were then post weld heat treated at 1033 K (760 °C) for 2h. Cross-sectional samples of as-TMT, TMT + tempered, and GTAW, GTAW + PWHT samples were prepared by using a conventional metallographic sample preparation, and characterized with different instruments. The samples were characterized on a JEOL 6500 FEG-SEM at 20 kV, using a Bruker Quantax EBSD (electron backscatter diffraction) Detector®. The GTAW and GTAW + PWHT samples were imaged for qualitative comparison using the same electron microscope. The as-TMT and TMT + temper second-phase (MX) size, density, and volume percent was characterized by traditional carbon-extracted replica technique. The high magnification observation was conducted by using a Zeiss Libra® 200 HT FE transmission electron microscope (TEM) equipped with a scanning-transmission electron microscope (STEM) mode with an accelerate voltage of 200kV and a spot size of 5nm. The carbides were identified by composition achieved by Energy-Dispersive X-ray Spectroscopy (EDS). The small particles (< 60 nm) in as-TMT and TMT + temper were assumed to be MX as they were enriched in Nb and V, and the larger particles (> 60 nm) in TMT + temper were assumed to be M<sub>23</sub>C<sub>6</sub> as they were enriched in Cr, which is consistent with literature [19-21]. Micro-Vickers hardness measurements were conducted on cross-sections of the GTAW + PWHT samples, using a 300g load for 12 seconds and automated stage motion, measuring hardness in 50-100µm steps across the base metal, heat affected zone, and weld metal. For creep-rupture testing, standard cross-weld tensile specimens with a cylindrical gauge section (ASTM E8) with 6.4mm diameter and 31.8mm length were machined from the GTAW + PWHT samples, and then tested at 873 K (600 °C) and 100MPa in laboratory air. Charpy V-notch impact testing (ASTM E23) was conducted at room temperature on standard size specimens (10mm x 10 mm x 55mm, with a 2mm depth V-notch) machined from the TMT + tempered sample. **The orientation of the Charpy impact test was parallel to the direction of deformation in TMT (i.e. forging direction).**

### 3. Results and Discussion

#### 3.1 Thermo-mechanical treatments

Figure 2 shows the microstructure of as-TMT and TMT + tempered samples, which were aus-forged with 7% thickness reduction and then aus-aged at 1173, 1073, and 973 K (900, 800, and 700°C) for 1h. Hereafter, these conditions will be called as “TMT9,” “TMT8,” and “TMT7,” respectively. The numbers corresponds to temperature in Celsius. Martensitic microstructure was observed in the as-TMT9 and as-TMT8 samples (see Fig. 2a and 2b), and they are macroscopically very similar to each other. The microstructures after tempering (see Fig. 2d and 2e) exhibited a typical tempered martensite of Grade 91 steels. The detailed observation indicated that a small amount of  $\alpha$ -ferrite grains formed in as-TMT8 sample (identified with black arrows in EBSD micrographs in section 3.2). The ferrite could have formed due to an increase in  $\gamma$  to  $\alpha$  transformation kinetics due to deformation and fine dispersion of MX precipitates (discussed in the present study) which could have promoted ferrite nucleation sites along the austenite matrix and grain boundaries [17]. On the other hand, instead of martensite, only mixed microstructure (ferrite + pearlite) was observed in as-TMT7 sample (see Fig. 2c) and, as a result, no drastic changes in microstructure were observed even after tempering (see Fig. 2f). These results indicate that in order to obtain martensitic microstructure the TMT process (i.e. with an isothermal hold of 1 h) needs to be conducted at or above 1073 K. Therefore, the sample from TMT7 was excluded from our studies. From here after, only data from TMT9 and TMT8 processing will be discussed in comparison of a standard normalized and tempered (N&T) heat treatment.

#### 3.2 Martensitic microstructure after TMT and pre-weld tempering

Because of the plastic deformation involved during TMT, microstructural factors such as prior austenite grain boundaries (PAGBs) and martensite block size could be affected in the present samples. It is well known that the PAGB and martensite block size are important constituents for strengthening due to the increased grain boundary area that restrict dislocation motion or possibly refine  $M_{23}C_6$  distribution [22-25]. The TMT process has not been extensively investigated in 9Cr steels, and most of the work has only described the enhancement of fine MX precipitation and does not compare martensitic microstructures [15, 16, 26, 27]. Figure 3 shows the EBSD patterns of the as-processed (a-c) and the as-tempered (d-f) microstructures. The images confirm typical martensitic microstructures as seen the optical micrographs above [9]. The PAGB and martensite block sizes are presented in table 2.

The trend illustrates that the TMT samples having finer PAGBs after processing. This is to be expected from deformation of the austenite grains, which will deform, recover, and produce smaller grains. However, the spread of the grain sizes (represented by the standard deviation) leads to the conclusion that the PAGBs have no significant differences. There was also not evidence of texturing in the samples, i.e. no elongated PAGBs were found. The conclusion can be presumed from the as-tempered PAGB sizes, where the differences between normalized and TMT samples is smaller. Note that decrease in PAGB after tempering is a consequence of the amount of measureable distinct (larger) PAGB is reduced after the tempering of martensite. While, the smaller PAGBs remain more distinct, thus, the measured average decreases.

As discussed above the possibility to a higher density of refined  $M_{23}C_6$  precipitates with increasing the grain boundary area of the PAGBs with deformation [28, 29]. However, it is determined that the grain boundary area of austenite has not significantly increased, which in turn would not lead to a greater density of fine  $M_{23}C_6$ . Furthermore, the martensite block sizes also does not indicate significant differences between standard N&T and TMT samples, which suggests that creep-rupture improvements would not be due to martensite grain size refinement. Thus, the conclusion can be made that the enhancement of creep-rupture properties can be attributed to the enhancement of the fine dispersion of MX and evolution of  $M_{23}C_6$  during tempering and welding, which will now be discussed. It is understood that the martensite lath size, also, can affect the creep strength. The average lath size was not measured in the present study because it could not be measured accurately through the EBSD analysis. However, based on the observed lath sizes in the EBSD analysis, it was assumed that no significant difference of the lath size exist among all the samples.

### ***3.3 Carbide microstructure after TMT and pre-weld tempering***

As discussed earlier, the microstructure and precipitate distributions before welding are the most important characteristics that controls creep strength. Yu et al. described a non-standard heat treatment that led to reduced size and volume percentage of  $M_{23}C_6$  carbides, but did not include MX precipitates [14]. The rational for the TMT is to produce a fine dispersion of small MX [i.e., carbonitrides] before tempering, which could minimize the formation of  $M_{23}C_6$ . Klueh et al. described that dislocations formed from deformation was chosen to act as nucleation site for MX during the aus-aging process [15, 16]. By precipitating the MX in the austenite phase during aus-aging, most of the carbon in austenite would have been tied up

with MX. As a result, during tempering the quantity of  $M_{23}C_6$  carbides would be reduced, either due to reduction of available alloying elements (e.g. carbon) or due to sluggish dissolution of small MX during tempering. Instead of coarsening, the carbon from the dissolved MX would then be available for  $M_{23}C_6$ . This would limit the nucleation and growth of  $M_{23}C_6$  [15, 16] during tempering and post-weld heat treatment.

Figure 4, represents STEM images of the carbon-extracted replica specimens taken from the as-TMT9 (see Fig. 4a), as-TMT8 (see Fig. 4b), and as-normalized (see Fig. 4c). The TMT9 and TMT8 samples illustrates the dispersions of nano-scale particles within the matrix after TMT. The particles were identified as MX from EDS, indicating enrichment of V and Nb. Higher magnification micrographs shows dense particles with the size of 5-10 nm dispersed in the as-TMT8 sample, which are qualitatively similar to the report by Klueh et al. [15]. On the other hand, a relatively smaller number of the particles can be seen in as-TMT9 sample. The average particle size, number density, and volume percentage are described in table 3. In both TMT conditions the average sizes are statistically very similar, but the number density and volume percent of TMT8 is more than 4 time higher than TMT9 and N&T samples. In addition, the size of the MX is about 2 times smaller than the MX that precipitates during standard N&T after tempering. This result indicates that the kinetics of MX formation during TMT process can be drawn as a C-curve with a nose close to 1073 K (800 °C) in a time-temperature-transformation (TTT) diagram, and 1173 K (900 °C) being closer to the upper temperature limit for expecting the MX formation during aus-aging for 1 hour. It should be noted in Fig. 4b, an inhomogeneous distribution of MX can be seen forming “cloud” like conglomerates. This is hypothesized to be the result of the inhomogeneous dislocation substructure after the TMT process [15]. Since dislocations as nucleation sites, locally higher density regions of dislocations would be expected to precipitate increased quantities of MX. Additionally, it must be noted that in the as-normalized N&T sample only large MX particles can be found. This is due to un-dissolving and coarsening of MX during manufacturing and normalization processes.

The differences from as-processed conditions can also be found in the as-tempered conditions. Figure 4d, 4e, and 4f shows the tempered conditions for TMT9, TMT8, and N&T samples respectively. Large particles and small particles can be visualized. The large particles ( $> 60$  nm) were identified as  $M_{23}C_6$  and the small particles (5-40 nm) were identified as MX. The particles were identified as their carbide type based on EDS. The large particles were enriched in Cr and the small particles were enriched in V and Nb. The tempered conditions of

TMT9 and N&T show similar  $M_{23}C_6$  carbide size and number density. The size of the  $M_{23}C_6$  carbide in these conditions is nominally 140 nm and the number density is nominally  $\sim 10^{20}$  particles/m<sup>3</sup>. It was concluded that the number density of MX in the as-processed condition of TMT9 did not successfully reduce the number of  $M_{23}C_6$ , although the number density of MX in TMT 9 is slightly higher than the N&T sample. This result is reflected in the creep curves (to be described in section 3.6). TMT9 had only slightly improved creep-rupture life over the N&T sample, which could be from the slight increase of MX in the matrix. In this condition, the volume percent of  $M_{23}C_6$  in TMT9 and N&T are very close to the equilibrium value. Utilizing the thermodynamic simulation software, JMatPro<sup>®</sup>, the equilibrium value of  $M_{23}C_6$  at the tempering temperature (1033 K (760 °C)) is calculated to be roughly 1.7 vol. % and the values measured in this work are, 1.5 vol. % for TMT9 and 1.4 vol. % for N&T. In contrast, the volume percent in TMT8 was 0.31%, which is almost 5 times smaller. In addition to the  $M_{23}C_6$  volume percent reduction, the MX density was much higher than TMT9 and N&T samples. Although the size of the MX is very similar to TMT9, the MX density is almost 2 times higher than TMT 9 and 3 times higher than N&T. Because of the amount of MX precipitated in the as-processed condition, we expect that MX particles may be carbon rich, and would prevent  $M_{23}C_6$  formation. Therefore, the absolute volume percentage of  $M_{23}C_6$  is reduced below the equilibrium value. This reduction in size and density of the  $M_{23}C_6$  would lead to more complete dissolution of the  $M_{23}C_6$  on heating to a peak temperature during welding and subsequently, fresh  $M_{23}C_6$  will re-precipitate along the fresh martensite/ferrite grain boundaries in the FGHAZ during PWHT, which is expected to improve the creep strength [14].

Figure 5 illustrates the MX and  $M_{23}C_6$  particle size distribution in the as-processed and as-tempered conditions. Because the N&T sample only contains residual particles and does not contain precipitated MX particles, this sample was not included in as-processed MX distribution. The overall range of sizes between TMT9 and TMT8 does not deviate much, with only the relative increased amount of particles in TMT8 illustrated. In addition, the as-tempered condition also shows very little deviation of the size range of MX in TMT9, TMT8, and N&T. Here also, the N&T sample contains a reduced amount of MX compared to the TMT samples, **which could be due to size coarsening of MX with decreasing the number density.** From table 3, the volume percentage for N&T and TMT8 appears to be equivalent. This is due to the particle size of MX in the N&T sample that leads to the calculated volume percent. Based on the creep data and discussions to be presented later, it is concluded that the

number density of MX particles plays a critical role in creep strengthening, rather than volume percent. When comparing the results from as-processed and as-tempered condition, the data suggest that MX is stable and does not coarsen during tempering. The stability of MX has been confirmed elsewhere [1, 19, 21, 28]. Conversely, to MX, the size distribution range of  $M_{23}C_6$  changes among samples. Similarly, the size and number density of  $M_{23}C_6$  in TMT9 and N&T sample are comparable. The data shown in Fig. 6 confirms that there are a large number of particles coarser than 120 nm. Several reports indicate that large particles can lead to creep cavitation and subsequent crack propagation [30-34]. Furthermore, with a larger fraction of coarser  $M_{23}C_6$ , we can speculate that these particles may not dissolve during welding and consequently coarsen further during PWHT. However, TMT8 shows a relatively small fraction of  $M_{23}C_6$  and particles larger than 180 nm. Therefore, it can then be suggested that most of the  $M_{23}C_6$  carbides will dissolve during welding and re-precipitate during PWHT. Therefore, the creep-rupture life is expected to increase with the decoration of ferrite grains by carbides and by preventing large carbide particles within the ferrite matrix [1, 14, 33].

### **3.4 Mechanical Heterogeneity of Welds**

Figure 6 illustrates cross-sectional micrographs of sample plates [N&T see Fig. 6a, TMT9 + temper see Fig. 6b, and TMT8 + temper see Fig 6c] with a single pass GTAW then a standard heat treatment (tempering at 1033 K (760 °C) for 2 hours) was applied. The cross-sectional microstructures consist of the weld metal, the heat affected zone, and the base metal, and there are no significant differences in the configurations among the samples. Overlaid onto the samples are corresponding micro-Vickers hardness maps. The standard N&T sample shows a high hardness weld metal with moderate hardness in the base metal. However, there is a distinct soft zone, which corresponds to the FGHAZ. Yu et al. described this region to correspond to coarse  $M_{23}C_6$  formation on “ghost” PAGBs resulting in ferrite grain boundaries being devoid of carbides [11, 14]. The TMT9 + tempered sample also exhibited a similar distinct softening zone. The creep-rupture of the cross-welded specimens is typically expected in this area. The soft zone in the FGHAZ indicates that TMT9 is not beneficial from the mechanical properties perspective. Conversely, the TMT8 + tempered shows only a distinct soft zone. Higher hardness ( $> 230$  VHN) is evident in the base metal whereas the other samples show lower hardness ( $< 210$  VHN) in the base metal. This high hardness in TMT8 sample is attributed to the precipitation hardening due to the dense MX formation [15,

16]. In addition, the TMT8 + tempered samples also showed lower softening in FGHAZ. This is attributed to the possible differences in carbide precipitations. Previous studies revealed that the RT hardness profile could reflect, but not predict, the high temperature creep resistances. Based on this empirical correlations, we expect improved creep properties would also be expected in the TMT8 + tempered sample [11, 35].

### ***3.5 FGHAZ precipitate evolution during welding and subsequent PWHT***

Microstructures of the as-welded and PWHT conditions were investigated. Figure 7 illustrates the microstructures of the FGHAZ in the as-welded and PWHT conditions after a GTAW with single bead, without filler metal, was applied. In Figure 7a, 7b, and 7c the as-welded microstructure still resembles the martensitic substructure. Some large undissolved carbides can be distinguished. In all the samples, the carbides are all less than 1  $\mu\text{m}$ . From the discussion above, the larger particles are assumed to be the undissolved  $\text{M}_{23}\text{C}_6$  carbides [9, 11, 14]. The smaller particles may be assumed to be some of the larger dispersion of MX particles, which can be seen in the TMT samples. Furthermore, fewer MX particles can be seen in the N&T sample. This demonstrates the larger volume percentage of MX in the TMT samples.

Due to the nature of the welded sample, extraction replicas could not be made as a function of spatial coordinates. Therefore, in this paper only qualitative analysis is made from the comparison of the as welded and as PWHT conditions from the SEM images. In the as welded condition for all the samples, the carbide structures seem similar in size and distribution. However, after the PWHT, different microstructures are now discernible. In all the samples, the traditional ferrite fine grains have formed. The large undissolved  $\text{M}_{23}\text{C}_6$  particles are seen in TMT9 and N&T samples are assumed to be possible “ghost” PAGBs. Because  $\text{M}_{23}\text{C}_6$  carbides form on PAGBs and these boundaries tend to be straight, the straight arrangement of large  $\text{M}_{23}\text{C}_6$  particles was identified as the “ghost” PAGBs. Yu et al. described ghost PAGBs as the line of carbides that had precipitated on the pre-weld PAGB [14]. During the welding cycle, new austenite grains form on heating and then form martensite creating new PAGBs on cooling. The  $\text{M}_{23}\text{C}_6$  carbides that do not dissolve stay in the original position of the pre-weld PAGB. In Figure 7d and 7f, possible ghost, PAGBs are shown with white arrows. TMT8 exhibits very few ghost PAGBs after the PWHT. The few ghost PAGBs that are still visible in TMT8, are smaller in length and size. Therefore, as seen

in Figure 7e, the ferrite grain boundaries are more decorated than the TMT9 and N&T samples. With carbides decorating the ferrite grains, grain boundary sliding could be minimized for longer period of time, possibly delaying creep deformation [10, 33, 36]. The carbide formations and free ferrite grain boundaries of TMT9 and N&T may allow for grain boundary sliding. This creates increased stress at the carbide/matrix boundary, which has been shown to produce creep cavitation on this boundary [30-32]. In addition to the re-distribution of  $M_{23}C_6$ , the effects of the enhanced MX should also be stressed. As discussed above, the TMT process will enhance the precipitation of MX. With MX being more stable, the MX should remain undissolved or only slightly coarsen during welding and post-weld heat treatment. This increased amount of MX will act as inhibitors to dislocation deformation during creep. The combination of these two mechanisms is expected to increase the cross-weld creep strength.

### ***3.6 Creep-rupture improvement***

The graph shown in Figure 8 illustrates the **creep and creep rate curves** of both TMT + tempered samples after GTAW and PWHT, together with those of the standard (N&T) and non-standard heat-treated samples after GTAW and PWHT [9, 11, 14]. The appearances of the creep-ruptured specimens of both TMT + tempered samples are also shown in Figure 8C. The samples were crept at 873 K (600 °C) and 100 MPa. **The cross-weld creep specimens were welded perpendicular to the deformation direction.** TMT9 + tempered failed at 1859 hours. This exhibits little improvement over the standard N&T sample. The slight increase in creep life can be attributed to the increase particle density of MX in TMT9. It is well known that MX is a large contributor to creep strength [1, 2, 8, 10, 14, 19, 21, 28, 34]. Thus, a slight increase in MX density would lead to a slight increase in creep life. However, the TMT8 + tempered shows improvement of the cross-weld creep properties. The sample failed at 2831 hours, which is almost double the creep life of N&T sample. The instantaneous creep rates (see Fig. 8b) were calculated by using the data from Fig. 8a using a moving linear slope fitting methodology. The plots show that in all samples, at the early stages of testing (< 100 h), the creep rate decreases consistent with primary creep stage. As expected, the N&T sample reaches a minimum creep rate of  $2 \times 10^{-7} \text{ s}^{-1}$  within 466 hours and quickly transitions to tertiary creep and failure within 1000 hours. The minimum creep rate slowly decreases by an order of magnitude to a value of  $2 \times 10^{-8} \text{ s}^{-1}$  with different processing conditions namely TMT9, TMT8, and NT650. Interestingly, all the cross-weld samples show two to three orders

of magnitude higher creep rate ( $10^{-7}$  and  $10^{-8}$  s $^{-1}$ ) than that of base metal ( $10^{-10}$  s $^{-1}$ ) reference sample. It must be noted that the creep strain and rates observed correspond to the overall strain of the entire sample, including the weld, HAZ, and base metal. Consequently, the creep rates do not show the actual rates for each zone of the material and suggests that the creep rate for the FGHAZ is underestimated and the creep rate for the base metal is overestimated here. This point is further addressed in section 3.7B.

From the Figure 8c crept specimens, the creep failure of both TMT + tempered samples took place at FGHAZ, indicating that the creep properties at FGHAZ dominated the creep deformation of these samples. With all the microstructural factors, discussed above, it can be concluded that the observed differences in cross-weld creep data are correlated with differences in the initial microstructure (size distribution of MX and M<sub>23</sub>C<sub>6</sub> precipitates) of base metal, as well as, spatial variations of the same within a cross-weld sample. In the next section, the observed creep rates are rationalized based on published theories for creep resistance.

### ***3.7 Rationalization of Creep Properties***

It was discussed above that the precipitation of MX was enhanced after TMT and an austenitizing process. As a result, an increased number density of MX remains through pre-weld tempering, weld thermal cycle and post weld heat treatment. Furthermore, in the previous sections, we also noticed marked differences in M<sub>23</sub>C<sub>6</sub> carbide size distribution. Since the creep deformation mechanism in Cr-Mo steels have been attributed to dislocation creep, the effects of TMT on creep resistance can be postulated. It is well known that particles impede the motion of dislocations (described above). Therefore, by increasing the density of particles through TMT, it can be expected that the dislocation motion would further be impeded. The minimum creep rate after TMT at 1073 K (800 °C) is reduced ( $4.8 \times 10^{-8}$ ) when compared to that of the standard N&T sample ( $2.8 \times 10^{-7}$ ). Although, the mechanisms described above may only partially represent the true reduction in minimum creep rates for a welded sample. As mentioned above this model does not examine the FGHAZ, therefore the overall creep improvements cannot entirely be described here. The above statements lead to two fundamental questions: (i) is it possible to correlate the minimum creep rate to precipitate distributions using published phenomenological models; and (ii) what is the role of strain localization in the FGHAZ?

**A. Phenomenological Model:** Shrestha et al. [37] have described the creep deformation mechanisms utilizing a modified Bird-Mukherjee-Dorn (BMD) equation, which incorporates a threshold stress, seen below [37].

$$\frac{\dot{\varepsilon}_m kT}{DEb} = A_{Dis} \left( \frac{\sigma_a - \sigma_{th}}{E} \right)^n \quad (1)$$

Where  $\dot{\varepsilon}_m$  is the minimum creep rate in the units of  $s^{-1}$ , D is the diffusion coefficient corresponding to self-diffusion of iron calculated using the following relationship.

$$[D = D_0 \exp\{-Q_0/RT\}] \quad (2)$$

Furthermore, R is the gas constant, E is the shear modulus, b is the burger vector length of edge dislocation in bcc iron lattice, k is the Boltzmann's constant and T is temperature in Kelvin.  $A_{Dis}$  and stress exponents n are parameters often calibrated through published data.  $\sigma_a$  is the measured stress value and  $\sigma_{th}$  is the threshold stress required to overcome the particle distribution. The threshold stress then takes into account the interparticle spacing  $\lambda$  and particle size  $d_{part}$  by the following equation taken from Ashby [38].

$$\sigma_{th} = \frac{Eb}{2\pi\lambda} \ln \frac{d_{part}}{b} \quad (3)$$

Utilizing this phenomenological BMD model, it is possible to evaluate the minimum creep rate in a sample with uniform microstructure defined by precipitate diameter and interparticle spacing. Typical parametric calculations using range of precipitate diameters (10 nm to 150 nm) and interparticle spacing (100 nm to 500 nm) are overlaid with experimentally measured minimum creep rates (see Fig. 9a) and particle size and spacing (see Fig. 9b). Note these are not specific to MX or  $M_{23}C_6$  from the study. Although it is known that the stress exponent n changes from  $>5$  to 1 at a particular point (with a decrease in stress) on a creep rate vs. stress plot, here the transition occurs where the tensile stress becomes larger than the threshold stress. **Figure 9a shows the parametric calculation dropping off at the point of this transition, revealing the transition is also sensitive to the particle sizes and spacing. Furthermore, since the measured particle distribution does not cross the transition, and the inhomogeneities of the cross-weld specimen, it makes it difficult to model the entirety of the mechanisms here.**

The plots demonstrate that experimentally measured creep properties and precipitate (both  $M_{23}C_6$  and MX precipitates) lie in a very sensitive area. A small change in particle diameter or spacing may lead to large changes in minimum creep rate of bcc ferrite matrix. This is evident in the white dash ovals (see Fig. 9b) which represents a theoretical range of MX or

$M_{23}C_6$  one could expect after different processing conditions and errors due to experimental measurements. The plot also shows experimentally measured precipitate characteristics (see Table 4) at different stages, i.e., as tempered, FGHAZ region after the post-weld heat treatment before creep testing, and at a FGHAZ failure location after creep testing. As expected, the number density of MX and  $M_{23}C_6$  reduced with concurrent increase in diameter of the particle, which results in higher interparticle spacing. The figure represents the evolution of the  $M_{23}C_6$  during welding, PWHT, and subsequent coarsening during creep. Although the particle distribution at the point of the minimum creep rate, Figure 9b shows, a relative correlation with the increase in creep rate at the  $M_{23}C_6$  is coarsening. Although the particle distribution at the minimum creep rate is not known, the figure can still show the evolution of creep rates with time. It should be noted that TMT8 (Crept) has a larger interparticle spacing than TMT9 (Crept). This is from maintain TMT8 for a longer time at temperature. Thus, the already low density of  $M_{23}C_6$  becomes coarser and the interparticle spacing increases. The above analyses show that the local creep rate of ferrite matrix is strongly a function of collective and spatial heterogeneity of precipitates (both MX and  $M_{23}C_6$ ) that evolves during each and every step of manufacturing operations, including welding. This is further discussed in the next section.

**B. Relevance of the BMD models to Cross-Weld Creep Samples:** It is important to note that the BMD model is developed for creep samples with uniform microstructures and without any gradients in microstructures. Therefore, extensions of the BMD model to cross weld creep testing requires discussion. Based on data from Figures 6 and 7, it is obvious that there would be a spatial variation of particle size and number density along the length of the cross weld creep testing sample. As a result, during creep testing, each and every part of the cross weld sample may exhibit different creep response leading to strain localization. Unfortunately, the standard creep testing measures only the overall length change and is not sensitive to strain concentrations in the FGHAZ region. This issue was recently addressed by Yu et al. through the use of digital image correlation (DIC) during early stages of creep testing of HTT and LTT samples at 923 K (650 °C) and 70 Mpa [11]. In their work, the strain localization at the early stages of creep testing (< 100 h) was observed in FGHAZ region on both left and right side of the weld metal region at a temperature. Corresponding strain rates have been calculated using the data. Their results show that the localized creep rate of the FGHAZ [ $5.64 \times 10^{-6} \text{ s}^{-1}$ ] and HTT sample is one order of magnitude greater than FGHAZ of LTT [ $6.67 \times 10^{-7} \text{ s}^{-1}$ ]<sup>†</sup>. The above analyses clearly demonstrate that the correlation

of observed creep rate in cross weld samples will require spatial and transient measurement of microstructure and creep rate. This is the focus of the ongoing investigation at the authors' institution. Nevertheless, the cross-weld testing with TMT samples have shown better creep resistance than welds made with standard heat treatments.

### **3.8 Room temperature toughness**

As described above, it is necessary that not only the creep strength be enhanced; the room temperature toughness should also be acceptable. As described above, the non-standard heat treatment (923 K (650 °C)/2hours) greatly improved the creep strength of 9Cr steel; however, the toughness was insufficient for real life deployment. The TMT process is intended to enhance the creep-rupture properties as well as maintaining sufficient RT toughness required for service. Figure 10 illustrates the RT (296 K (23 °C)) toughness of TMT8 + tempering compared to standard N&T and the non-standard HT. **It must be noted that the sample used in the Charpy impact test was from another experiment from the authors.** The sample here was aus-rolled at 1073 K (800 °C) with 17% thickness reduction, followed by aus-aged at 1073 K (800 °C) for 1h [12]. The average Charpy impact absorbed energy of the TMT8 + tempered sample was more than 150J **at 296 K (23 °C).** Although the deformation was greater than that of sample described in the current study, the toughness is expected to be similar for all TMT samples because of the application of the standard tempering (1033 K (760 °C)/2hours) and similar microstructure. Therefore, the TMT process at 1073 K (800 °C) combined with a standard tempering can be described as an optimized TMT process to achieve improved cross-weld creep properties together with sufficient room-temperature toughness of the base metal.

## **4. Conclusions**

Suitability of thermo-mechanical treatment of the Grade 91 (Modified 9Cr-1Mo, ASTM A387) steel for improving cross-weld creep performance at 873 K (600 °C) and 100 MPa, as well as, room temperature toughness was evaluated. Detailed microstructure characterization revealed a strong correlation between MX and M<sub>23</sub>C<sub>6</sub> precipitate distributions to cross-weld creep properties based on the following findings.

- (1) The TMT at 1073 K (800 °C) + temper sample did not show significant reduction of the hardness at the FGHAZ after welding and PWHT. Since the prior austenite grain size and

martensite block widths were found to be similar in all samples after thermo-mechanical processing, as well as, after standard heat treatments, the reduced HAZ softening is correlated with fine distribution of MX and  $M_{23}C_6$  precipitates within fresh martensite/ferrite grains. Since creep failure is observed in the FGHAZ, minimization of the coarsened  $M_{23}C_6$  could also lead to the improved creep strength.

- (2) The samples subjected to TMT at 1073 K (800 °C) also exhibited lower minimum creep rate ( $4.8 \times 10^{-8} \text{ s}^{-1}$ ) even after standard pre-weld tempering, welding, and post weld heat treatment, in contrast to samples ( $2.04 \times 10^{-7} \text{ s}^{-1}$ ) without thermo-mechanical processing. In addition, the time to creep rupture failure (~2700 h) of this sample was higher than that of (~1400 h) standard heat treatment.
- (3) TMT processing could not eliminate the Type IV failure. Detailed analyses of precipitate size distributions, minimum creep rate, phenomenological creep models, and published localized creep strains indicate that type IV cracking is the manifestation of spatial and temporal evolution of precipitate size distribution and its influence on the dislocation creep within the bcc-ferrite matrix.
- (4) The base metal of the samples after the TMT at 1073 K (800 °C) + standard tempering (1033 K (760 °C) for 2hr) showed sufficient room-temperature Charpy impact toughness that was comparable to the standard heat-treated samples.
- (5) The above results confirmed our hypotheses that the TMT process is indeed a viable path to improve cross-weld creep resistance at high temperature, as well as, toughness at low temperature.

## ***5. Acknowledgements***

The authors thank Drs. Xinghua Yu and David T. Hoelzer at Oak Ridge National Laboratory for their comments on this manuscript. Research sponsored by the Crosscutting Research Program, Office of Fossil Energy, U.S. Department of Energy.

## **6. References**

1. Abe, F. *Science and Technology of Advanced Materials*, 2008. **9**(1): p. 013002.
2. Bhadeshia, H.K.D.H. *Isij International*, 2001. **41**(6): p. 626-640.

3. Yu, X. Doctor of Philosophy Dissertation, Columbus, Ohio: The Ohio State University, 2012.
4. Auerkari, P., et al. International Journal of Pressure Vessels and Piping, 2007. **84**(1-2): p. 69-74.
5. Hirata, H. and K. Ogawa. Welding International, 2005. **19**(2): p. 118-124.
6. Hirata, H. and K. Ogawa. Welding International, 2005. **19**(2): p. 109-117.
7. Laha, K., et al. Metallurgical and Materials Transactions A, 2008. **40**(2): p. 386-397.
8. Tsukamoto, S., et al. Trends in Welding Research, 2009: p. 296-302.
9. Yukinori Yamamoto, et al. Proceeding of the 10th Liège Conference on Materials for Advanced Power Engineering, 2014.
10. Francis, J.A., W. Mazur, and H.K.D.H. Bhadeshia. Materials Science and Technology, 2006. **22**(12): p. 1387-1395.
11. Yukinori Yamamoto, Xinghua Yu, and S.S. Babu. Proceedings of the ASME Symposium on Elevated Temperature Application of Materials for Fossil, Nuclear, and Petrochemical Industries, 2014.
12. Shassere, B., Y. Yamamoto, and S.S. Babu. Proceeding of the International Conference on Solid-Solid Phase Transformations in Inorganic Materials, 2015.
13. Brinkman, C.R., Sikka, V.K., Horak, J.A., Santella, M.L. ORNL/TM-10504, 1987.
14. Yu, X., et al. Acta Materialia, 2013. **61**(6): p. 2194-2206.
15. Klueh, R.L., N. Hashimoto, and P.J. Maziasz. Scripta Materialia, 2005. **53**(3): p. 275-280.
16. Klueh, R.L., N. Hashimoto, and P.J. Maziasz. Journal of Nuclear Materials, 2007. **367-370**: p. 48-53.
17. Nöhrer, M., et al. Metallurgical and Materials Transactions A, 2014. **45**(10): p. 4210-4219.

18. Tamura, M., et al. Journal of Nuclear Materials, 2003. **321**(2-3): p. 288-293.
19. Sawada, K., K. Kubo, and F. Abe. Materials Science and Engineering a-Structural Materials Properties Microstructure and Processing, 2001. **319**: p. 784-787.
20. Hofer, P., H. Cerjak, and P. Warbichler. Materials Science and Technology, 2000. **16**(10): p. 1221-1225.
21. Taneike, M., K. Sawada, and F. Abe. Metallurgical and Materials Transactions a-Physical Metallurgy and Materials Science, 2004. **35A**(4): p. 1255-1262.
22. Maruyama, K., K. Sawada, and J. Koike. Isij International, 2001. **41**(6): p. 641-653.
23. Kawata, H., et al. Materials Science and Engineering: A, 2006. **438-440**: p. 140-144.
24. Morito, S., et al. Acta Materialia, 2003. **51**(6): p. 1789-1799.
25. Kitahara, H., et al. Acta Materialia, 2006. **54**(5): p. 1279-1288.
26. Song, S.M., et al., *Effect of TMT process on the strength and precipitation behavior of an 11Cr-0.3Mo-1.6W steel during long term aging*, in *Mechanical Behavior of Materials X, Pts 1 and 2*, S.W. Nam, et al., Editors. 2007, Trans Tech Publications Ltd: Stafa-Zurich. p. 1565-1568.
27. Li, S.Z., et al. Materials Science and Engineering a-Structural Materials Properties Microstructure and Processing, 2013. **559**: p. 882-888.
28. Abe, F., et al. Materials Science and Engineering: A, 2004. **378**(1-2): p. 299-303.
29. Abe, F. Metallurgical and Materials Transactions a-Physical Metallurgy and Materials Science, 2005. **36A**(2): p. 321-332.
30. Babu, S.S., et al. Metallurgical and Materials Transactions a-Physical Metallurgy and Materials Science, 1996. **27**(3): p. 763-774.
31. Li, D. and K. Shinozaki. Science and Technology of Welding and Joining, 2005. **10**(5): p. 544-549.

32. Watanabe, T., et al. International Journal of Pressure Vessels and Piping, 2004. **81**(3): p. 279-284.
33. Gupta, C., et al. Materials Science and Technology, 2015. **31**(5): p. 603-626.
34. Thomson, R.C. and H.K.D.H. Bhadeshia. Metallurgical Transactions a-Physical Metallurgy and Materials Science, 1992. **23**(4): p. 1171-1179.
35. Yu, X., Zhili Feng, and Y. Yamamoto. Proceedings of 7th International Conference on Advances in Materials Technology for Fossil Power Plants, 2013.
36. Smith, D.J., N.S. Walker, and S.T. Kimmins. International Journal of Pressure Vessels and Piping, 2003. **80**(9): p. 617-627.
37. Shrestha, T., et al. Materials Science and Engineering: A, 2013. **565**: p. 382-391.
38. Ashby, M.F. Acta Metallurgica, 1966. **14**(5): p. 679-&.

*List of Tables*

*Table 1: Chemical compositions (wt%) of the Grade 91 base metal and filler metal (balanced Fe).*

(wt%)	C	Mn	Si	Cr	Mo	Ni	V	Nb	N	B
Base metal	0.08	0.27	0.11	8.61	0.89	0.09	0.21	0.07	0.06	<0.001
Filler metal	0.08	0.41	0.31	8.62	0.92	0.15	0.24	0.08	0.04	<0.001

*Table 2 Average size of PAGBs and martensite blocks after processing and subsequent pre-weld temper (with standard deviations)*

	as-Processed PAGBS (μm)	as-Tempered PAGBS	as-Processed Martensite Block (μm)	as-Tempered Martensite Block (μm)
Normalized	31.2±9	24.5±9	4.5±2.5	4.3±2.1
TMT 9	21.3±5	19.7±6.7	4.4±2.3	5.2±2.3
TMT 8	20.1±5.5	19.1±3.8	5.0±2.5	6.0±2.5

*Table 3: Average diameter, number density and volume percentage of carbides in N&T, TMT9 + temper, and TMT8 + temper conditions. \*As normalized only contains undissolved large MX from austenization.*

	Carbide Type	Diameter (nm±3.26)	Number Density (m <sup>-3</sup> ±1.12x10 <sup>17</sup> )	Volume Percentage (%)
N&T As-Normalized	MX M23C6	110.0 N/A	.0093 x 10 <sup>20</sup> N/A	0.069±.008* N/A
N&T	MX M23C6	21.8 140.1	1.9 x 10 <sup>19</sup> 10.6 x 10 <sup>18</sup>	0.010±.002 1.530±.039
TMT 9	MX M23C6	7.9 N/A	1.75 x 10 <sup>20</sup> N/A	0.005±.002 N/A
TMT 9 + T	MX M23C6	13.9 147.2	2.81 x 10 <sup>19</sup> 9.7 x 10 <sup>18</sup>	0.004±.001 1.620±.040
TMT 8	MX M23C6	8.7 N/A	7.28 x 10 <sup>20</sup> N/A	0.025±.009 N/A
TMT 8 + T	MX M23C6	15.4 128.8	5.69 x 10 <sup>19</sup> 3.42 x 10 <sup>18</sup>	0.011±.002 0.383±.016

*Table 4: Average diameter, number density and volume percentage of carbides and interparticle spacing of MX and  $M_{23}C_6$  in HTT, LTT, TMT8, and TMT9 weld samples at FGHAZ before creep testing. In addition, the precipitate characteristics of TMT8 and TMT9 weld samples after creep testing.*

	Diameter (nm $\pm$ 15)	Number Density (m $^{-3}$ $\pm$ 3.93 x 10 $^{15}$ )	Volume Percentage (%)	Interparticle Spacing (nm $\pm$ 37.8)
N&T (HTT)	165.5	2.18 x 10 $^{18}$	.518	263.0
N&T (LTT)	152.6	3.20 x 10 $^{18}$	.594	223.7
TMT 9	156.4	2.22 x 10 $^{18}$	.525	315.2
TMT 9 (Crept)	214.2	1.56 x 10 $^{18}$	.800	317.2
TMT 8	147.2	2.55 x 10 $^{18}$	.425	322.7
TMT 8 (Crept)	213.8	1.01 x 10 $^{18}$	.515	396.7

## List of Figures and Captions

*Figure 1: Temperature profiles of the thermo-mechanical heat treatments studied.  $M_s$  and  $M_f$  corresponds to the calculated martensite start and finish temperatures respectively [9]*

*Figure 2: Optical microscopy images showing microstructure of as-TMT (a-c) and TMT + tempered (d-f) samples; the aus-forged and aus-aged temperatures were at 1173 K (900 °C) (a,d), 1073 K (800 °C) (b,e), and 973 K (700 °C) (c,f)*

*Figure 3: EBSD images showing microstructure of as-processed (a-c) and as-tempered (d-f) samples. The aus-forging and aging temperatures are shown above. Here TMT 900 and TMT 800 are compared to standard N&T treatments. The black arrows show the small ferrite formation described in section 3.1*

*Figure 4: Dark field STEM images of carbon-extracted replica specimens taken from the Grade 91 steel applied (a, d) TMT at 1173 K (900 °C), (b, e) at 1073 K (800 °C), and (c, f) N&T. In the as-processed condition of TMT specimens, a fine dispersion of MX can be found only in TMT8 (white spots are carbide/carbonitrides, black background is carbon support)*

*Figure 5: Particle size distributions of  $M_{23}C_6$  and MX precipitates in the as-processed and the as-tempered conditions*

*Figure 6: Cross sectional microstructure and hardness maps of the Grade 91 steel after (a) standard N&T, (b) TMT at 1173 K (900 °C) + PWHT, or (c) TMT at 1073 K (800 °C) + PWHT, followed by a single pass GTAW (no filler metal) + PWHT.*

*Figure 7: SEM images of single bead as welded and as PWHT sample specimens, (a,d) TMT at 1173 K (900 °C), (b,e) at 1073 K (800 °C), and (c,f) N&T. In the as-processed condition of TMT specimens, a fine dispersion of MX can be found, in N&T only MX remaining after austenization. In as tempered conditions possible ghost PAGBs can be delineated.*

*Figure 8: Measured (a) cross weld creep strain and (b) creep rate curves of samples tested at 873 K (600 °C) at a stress level 100MPa. The plots compare the data from TMT samples with the published data from standard and non-standard pre-weld tempering [8, 10]. The creep rate data is also compared with published creep rate of base metal grade 91 steel. (c) The failed samples show that, even with differences in creep resistance, the failure modes (along the FGHAZ) are similar in both TMT8 and TMT9 samples.*

*Figure 9: Results from parametric calculations of minimum creep rate using BMD phenomenological model as a function of (a) stress and (b) precipitate characteristics.*

*Figure 10: Charpy impact test results of the Grade 91 steel applied TMT at 1073 K (800 °C) + tempering, together with those of the standard and non-standard heat-treated samples [8].*

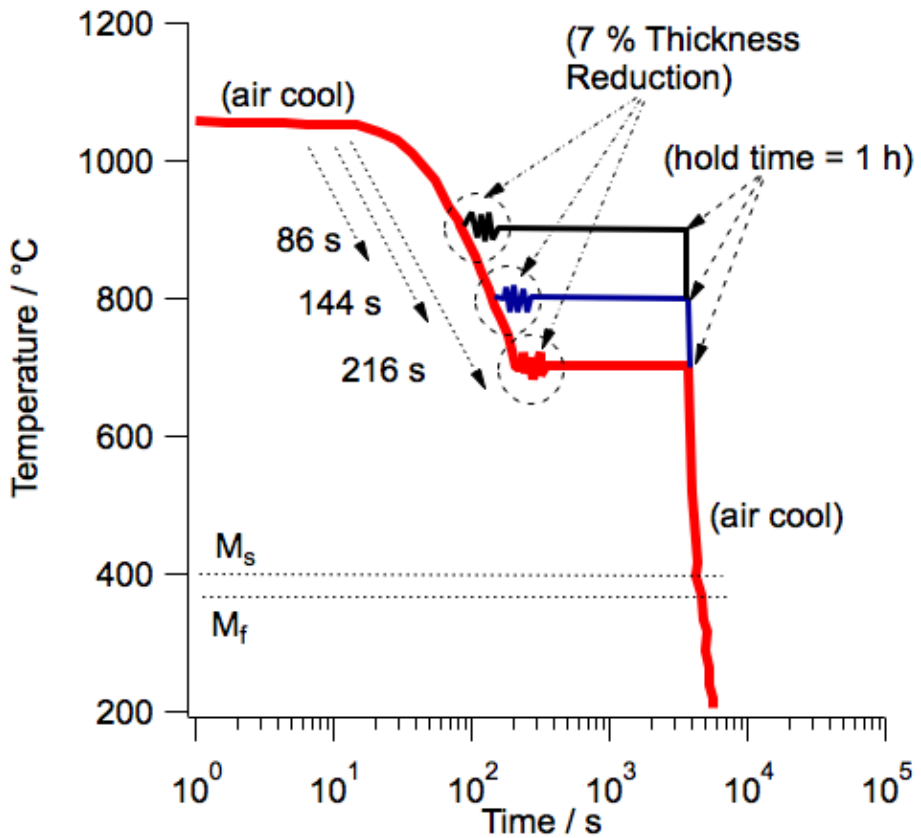


Figure 1: Temperature profiles of the thermo-mechanical heat treatments studied.  $M_s$  and  $M_f$  corresponds to the calculated martensite start and finish temperatures respectively [9]

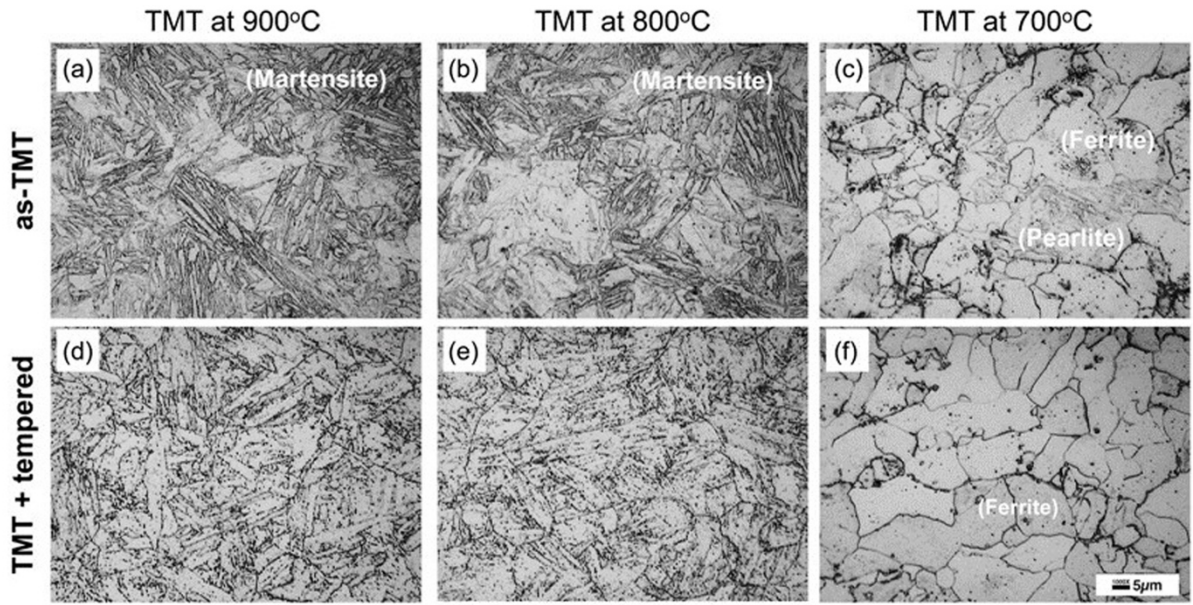


Figure 2: Optical microscopy images showing microstructure of as-TMT (a-c) and TMT + tempered (d-f) samples; the aus-forged and aus-aged temperatures were at 900°C (a,d), 800°C (b,e), and 700°C (c,f)

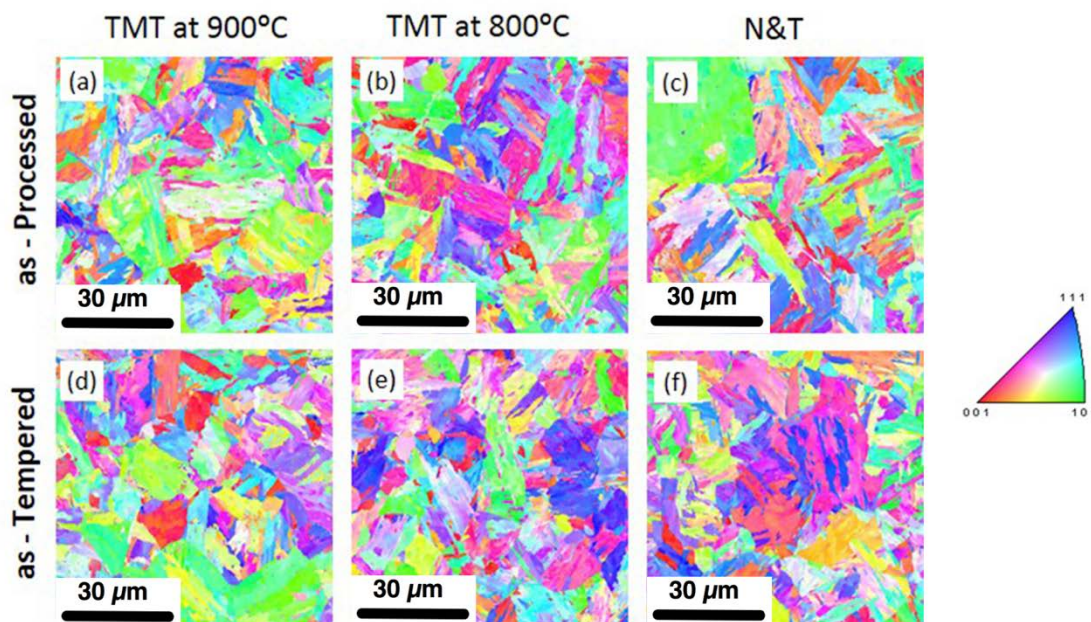


Figure 3: EBSD images showing microstructure of as-processed (a-c) and as-tempered (d-f) samples. The aus-forging and aging temperatures are shown above. Here TMT 900 and TMT 800 are compared to standard N&T treatments

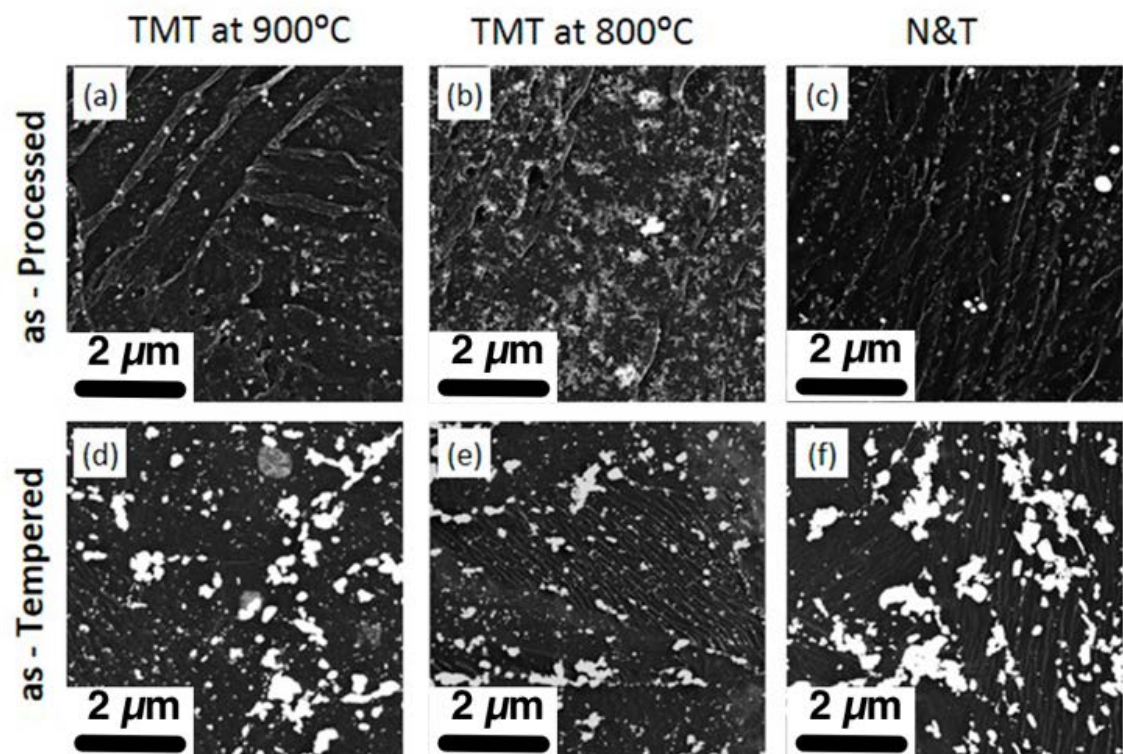


Figure 4: Dark field STEM images of carbon-extracted replica specimens taken from the Grade 91 steel applied (a, d) TMT at 900°C, (b, e) at 800°C, and (c, f) N&T. In the as-processed condition of TMT specimens, a fine dispersion of MX can be found only in TMT8 (white spots are carbide/carbonitrides, black background is carbon support)

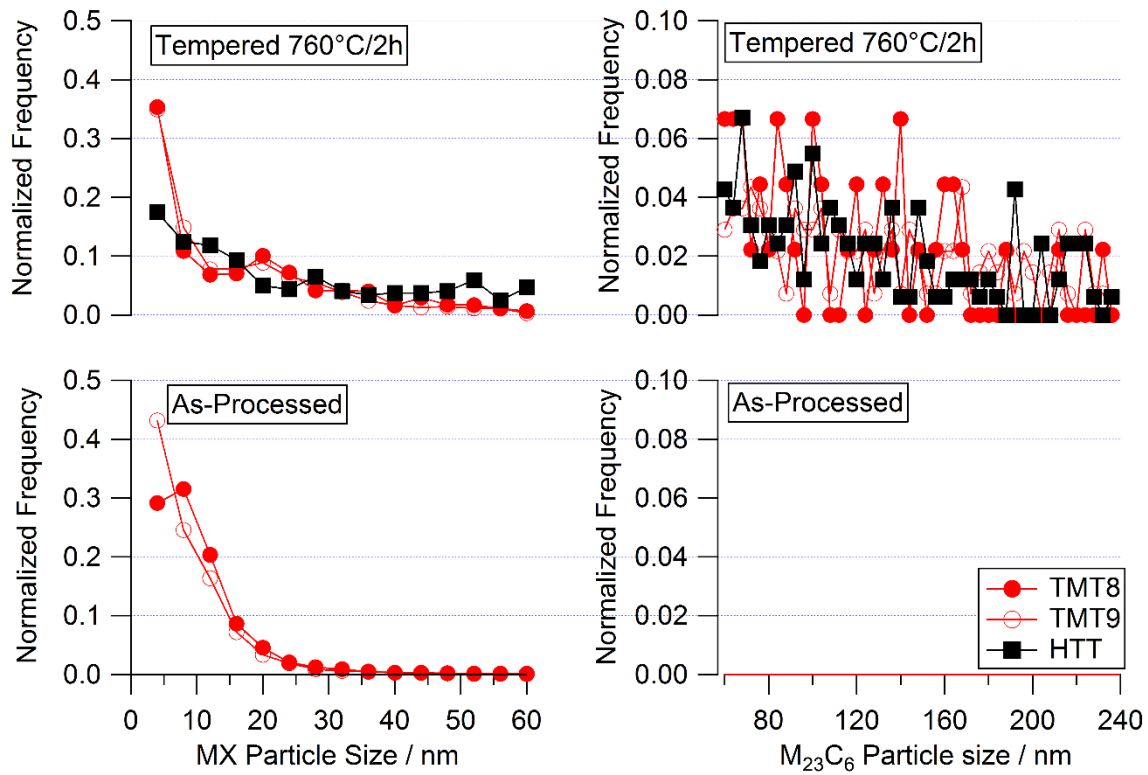


Figure 5: Particle size distributions of  $M_{23}C_6$  and MX precipitates in the as-processed and the as-tempered conditions

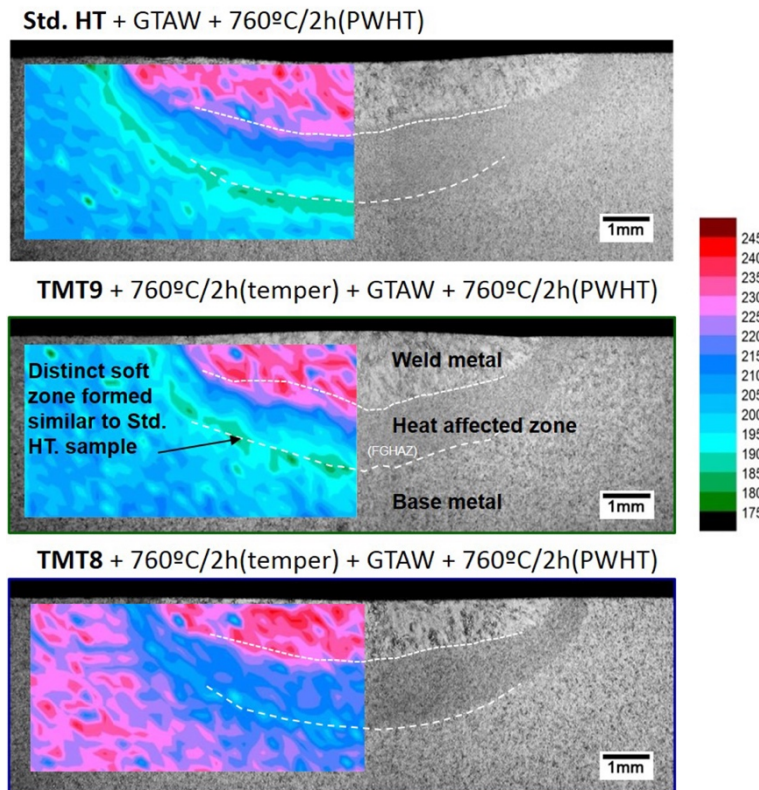
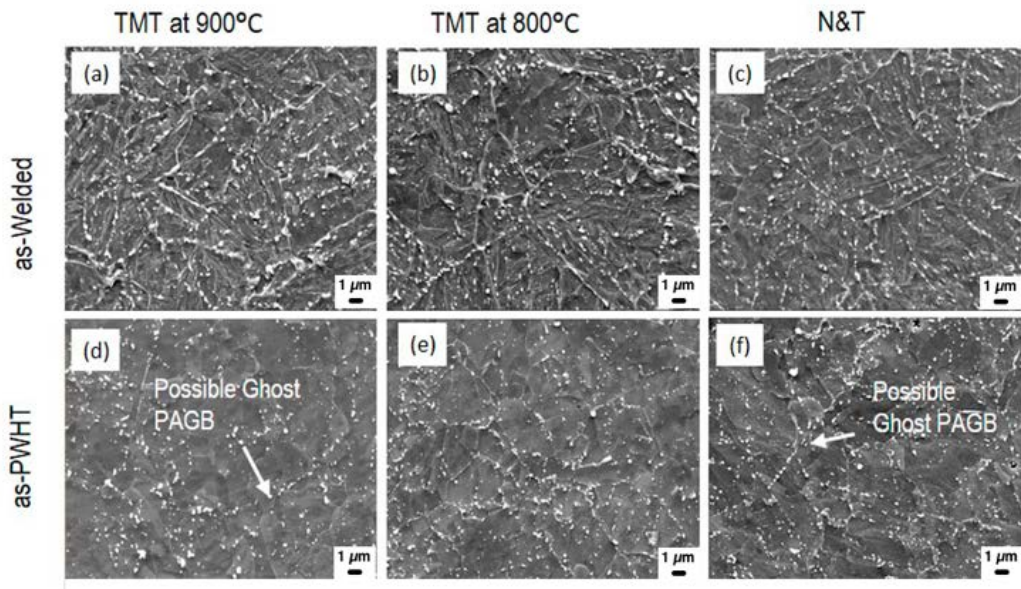


Figure 6: Cross sectional microstructure and hardness maps of the Grade 91 steel after (a) standard N&T, (b) TMT at 900°C + PWHT, or (c) TMT at 800°C + PWHT, followed by a single pass GTAW (no filler metal) + PWHT.



*Figure 7: SEM images of single bead as welded and as PWHT sample specimens, (a,d) TMT at 900°C, (b,e) at 800°C, and (c,f) N&T. In the as-processed condition of TMT specimens, a fine dispersion of MX can be found, in N&T only MX remaining after austenization. In as tempered conditions possible ghost PAGBs can be delineated.*

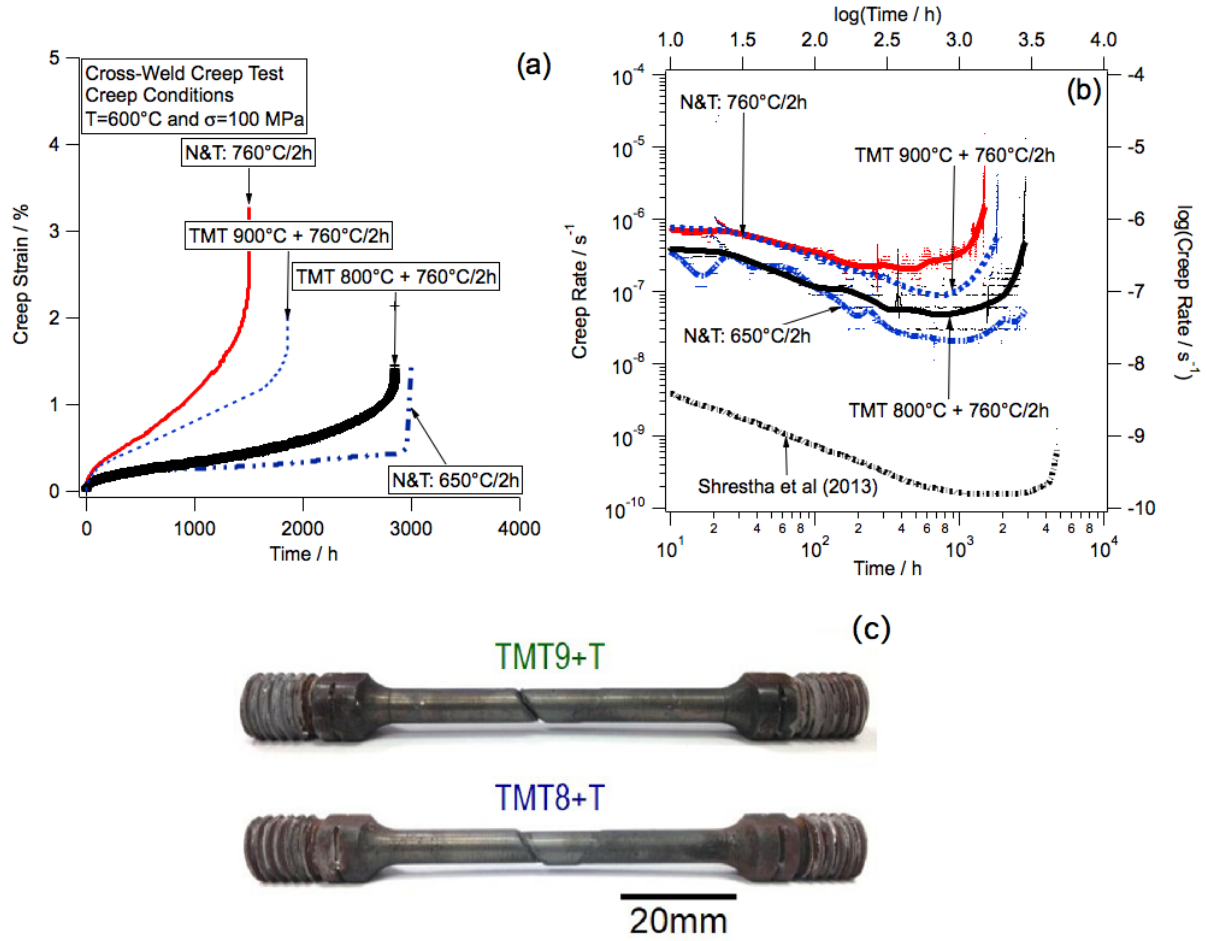


Figure 8: Measured (a) cross weld creep strain and (b) creep rate curves of samples tested at 600°C at a stress level 100MPa. The plots compare the data from TMT samples with the published data from standard and non-standard pre-weld tempering [8, 10]. The creep rate data is also compared with published creep rate of base metal grade 91 steel. (c) The failed samples show that, even with differences in creep resistance, the failure modes (along the FGHAZ) are similar in both TMT8 and TMT9 samples.

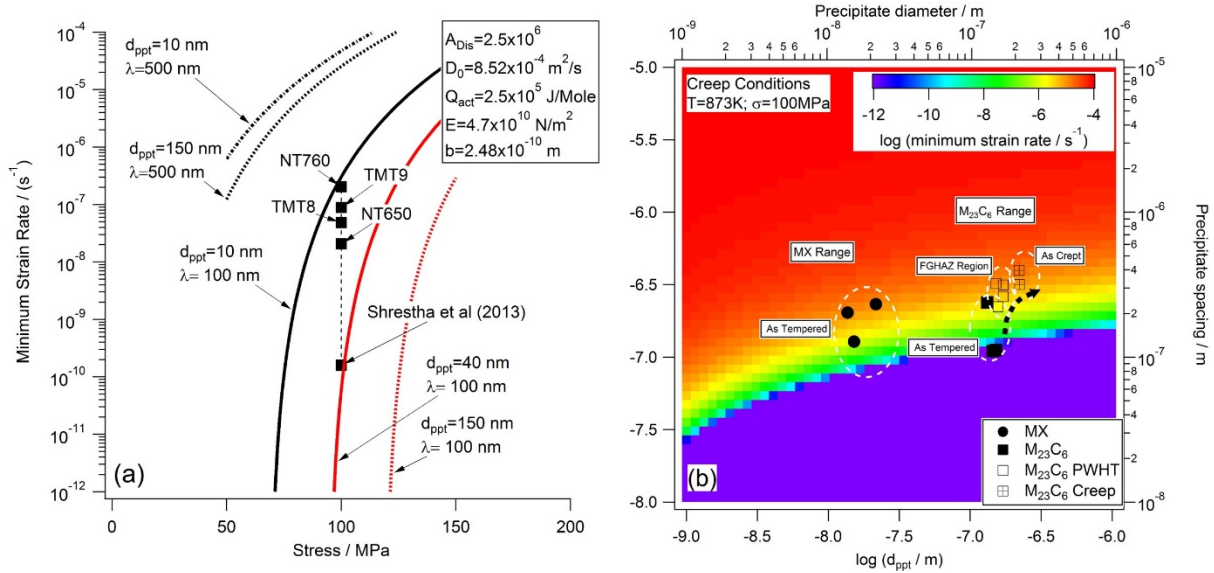


Figure 9: Results from parametric calculations of minimum creep rate using BMD phenomenological model as a function of (a) stress and (b) precipitate characteristics.

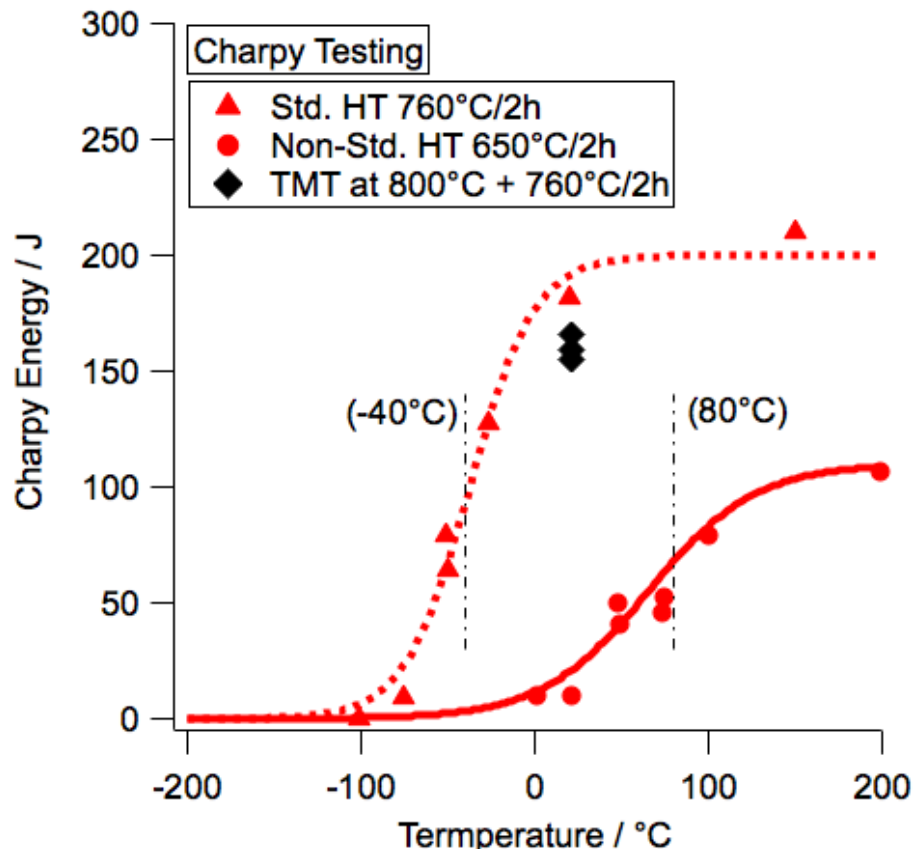


Figure 10: Charpy impact test results of the Grade 91 steel applied TMT at 800°C + tempering, together with those of the standard and non-standard heat-treated samples [8].